Model Reduction for a Variable Geometry Fluid Thermal Problem

Elliott Baché, Jose M. Vega, and A. Velázquez

Abstract—**A methodology is presented to create reduced models of fluid thermal problems with varying geometry. The methodology is applied to the nonisothermal backward-facing step problem, depending on three parameters: the Reynolds number, the wall temperature, and the step height. Various snapshots are calculated using a computational fluid dynamics (CFD) solver in disparate grids, which are transformed into a generic grid by means of a smooth function. A proper orthogonal decomposition basis is created for these transformed snapshots, the flow variables are expanded into the resulting modes, and the reconstructed flow variable distributions are transformed back into the original grids. The associated mode amplitudes are calculated minimizing (using a genetic algorithm) a residual, which is defined using a limited number of grid points (which lessens the computational effort). The resulting reduced order model provides solutions that compare well with their CFD counterparts, in a much smaller CPU time.**

Index Terms—**Proper orthogonal decomposition, variable geometry, reduced order model.**

I. INTRODUCTION

REDUCED order models (ROMs) are becoming more and more efficient and thus more appealing for industrial applications. Applications such as optimization and conceptual design can be easily handled with a ROM, reducing the time span from the beginning phase to the final phases of the design process. A review of advances in such ROMs is presented in [10].

Although ROMs are becoming widespread in many types of applications, there are not that many that deal with varying geometries. The varying geometry involves difficulties for example when applying proper orthogonal decomposition (POD). In order to surmount these difficulties, a few techniques have been proposed account for varying geometries, such as those presented in [3], [15], [17], [13], [8], [12], and [14]. Among these, the authors employ such methods as a multi-POD approach (using a POD basis for each grid deformation) and mapping the grid displacement as a parameter. There are however no cases where they create a POD basis with varying grids.

In this paper, a POD-based ROM that takes into account a variable geometry as one of the parameters will be developed. The paper is a continuation of the related former work by us [1], [2], which presented the same type of ROM but with fixed geometries.

E. Bache and A. Velazquez are in the Aerospace Propulsion and Fluid Mechanics Department, School of Aeronautics, Universidad Politecnica de Madrid, Plaza del Cardenal Cisneros 3, 28040 Madrid, Spain e-mail: elliottbache@hotmail.com angel.velazquez@upm.es

J. M. Vega is in the Applied Mathematics Department, School of Aeronautics, Universidad Politecnica de Madrid, Plaza del Cardenal Cisneros 3, 28040 Madrid, Spain. e-mail: josemanuel.vega@upm.es
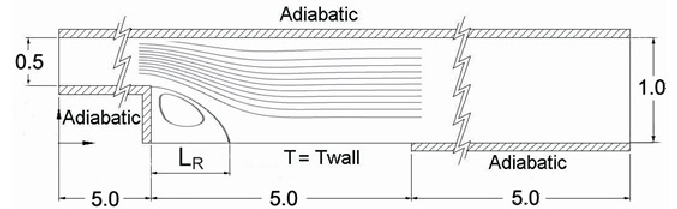
Fig. 1. Sketch of the test problem configuration. Flow goes from left to right.

II. APPLICATION DESCRIPTION

A. Flow Description

The test problem to illustrate the methodology is a 2D laminar, incompressible flow through a backward-facing step with a portion of the lower wall being heated. In the equations and boundary conditions below, all distances were rendered dimensionless using the hydraulic diameter of the inlet channel (twice the inlet height). The velocity, pressure, and temperature are non-dimensonalized with the mean inlet velocity, the inlet dynamic pressure, and the inlet temperature, respectively.

The governing equations are

$$\partial_x u + \partial_y v = 0, \tag{1}$$

$$u\partial_x u + v\partial_y u + \partial_x p - \frac{\mu\Delta u + 2\partial_x\mu\partial_x u(\partial_y u + \partial_x v)}{Re} = 0, \tag{2}$$

$$u\partial_x v + v\partial_y v + \partial_y p - \frac{\mu\Delta v + 2\partial_x\mu\partial_x v(\partial_x v + \partial_y u)}{Re} = 0, \tag{3}$$

$$u\partial_x T + v\partial_y T - \frac{\kappa\Delta T + \partial_x\kappa\partial_x T + \partial_y\kappa\partial_y T}{RePr} = 0, \tag{4}$$

where ∂_x and ∂_y stand for partial derivatives, $\Delta = \partial_{xx}^2 + \partial_{yy}^2$ is the Laplacian operator, and the inlet Reynolds and Prandtl numbers are defined as

$$\begin{aligned} \mathrm{Re} &= 2\tilde{\rho}_{inlet}\tilde{h}_{inlet}\tilde{u}_{inlet}/\tilde{\mu}(\tilde{T}_{inlet}), \\ \mathrm{Pr} &= \tilde{c}_p\tilde{\mu}(\tilde{T}_{inlet})/\tilde{\kappa}(\tilde{T}_{inlet}). \end{aligned} \tag{5}$$

Here, $\tilde{u}_{inlet}$ is the mean inlet velocity and tildes denote dimensional quantities. μ and κ are the dimensionless viscosity and thermal conductivity, which (in the considered temperature range, assuming that the working fluid is water) depend on temperature as $\mu = 1 - 5.646(T-1) + 12.26(T-1)^2$ and $\kappa = 1 + 0.786(T-1) - 1.176(T-1)^2$, which result from well known correlations [16].

The boundary conditions are as follows. At the inlet section, $x = 0$, the velocity profiles and pressure gradient are assumed to be Poiseuille-like and the temperature is set equal to the coolant temperature. At the outlet section, $x = 15$, the flow is also assumed to be fully developed and thus a stress

free condition is imposed, namely $\partial_x u = \partial_x v = \partial_{xx}^2 p = \partial_x T = 0$. At the walls, we impose noslip ($u = v = 0$), and the following thermal conditions $T = T_{wall}$ if $5 < x < 10.5$ and $y = 0$, and $u = v = 0, \partial_n T = 0$. Here, n stands for the direction normal to the wall.

The CFD computations needed to generate the snapshots are carried out with the solver described in [16]. Three free parameters are present, namely the Reynolds number, the wall temperature downstream of the step, and the step height. The maximum Reynolds number (400) is selected to preserve the hypothesis that the flow is two dimensional [16], [4], [7], and [5]. The step height is allowed to change in a rather wide range (0.1 to 0.6), which involves large changes in both the geometry and flow topologies. An idea of the severity of this change is provided in Fig. 2, where the streamlines patterns are shown for three representative cases. Solving the
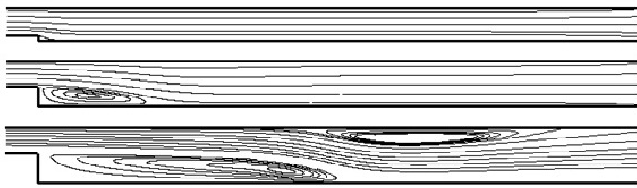

Fig. 2. Streamlines for the cases: $Re = 100, T_w = 1.0, H = 0.1$ (top), $Re = 200, T_w = 1.1, H = 0.4$ (middle), and $Re = 400, T_w = 1.2, H = 0.6$ (bottom).

problem also requires drastic changes in the computational mesh, both in the number of points (which are 6,347, 12,485, and 16,577 in the three cases considered in Fig.2) and in their distribution (which involves drastic changes of mesh size, see Fig.3). Initially, snapshots are computed for the following 210 combinations of parameters:

- $Re = 100, 150, 200, 250, 300, 350$, and 400,
- $T_w = 1.0, 1.05, 1.10, 1.15$, and 1.20,
- $H = 0.1, 0.2, 0.3, 0.4, 0.5$, and 0.6.

Later on (see below), one additional series of snapshots will be computed in the case $H = 0.15$ to improve results, which will increase the total number of snapshots to 245. To assess the ROM accuracy, a series of 10 test points has been defined inside the parametric space, see Table I. Three figures of merit have been chosen to compare the ROM and CFD results, namely the reattachment length, L_R, of the recirculation region located directly downstream of the step, the pressure drop, P_{drop}, between entrance and exit, and the heat flux across the heated portion of the lower wall behind the step (see Fig.1). The latter is accounted for using the heat flux per unit width, defined as

$$Q' = \sum \partial_y T(x, 0) \kappa(T(x, 0)) \qquad (6)$$

where Q' is the non-dimensional heat flux across the non-adiabatic part of the lower wall. The actual CFD values of these figures of merit at the test points are given in Table I

III. METHOD DESCRIPTION

A. Virtual grid

The mesh used in the CFD calculations is separated into 5 different zones, as plotted in Fig. 3-top. A close-up view

TABLE I
DEFINITION OF TEST POINTS AND CFD VALUES OF THE FIGURES OF MERIT

Test point	Problem parameters			Figures of merit		
	Re	T_{wall}	H	L_R	P_{drop}	$\tilde{Q}'$
P01	225	1.075	0.35	1.783	1.094	3.202
P02	275	1.125	0.45	2.917	0.727	5.347
P11	125	1.025	0.15	0.317	3.318	1.088
P12	125	1.175	0.15	0.383	3.026	8.702
P13	125	1.025	0.55	1.983	1.963	0.734
P14	125	1.175	0.55	2.167	1.910	5.980
P15	375	1.025	0.15	0.683	0.921	1.507
P16	375	1.175	0.15	0.817	0.836	12.21
P17	375	1.025	0.55	4.350	0.417	0.905
P18	375	1.175	0.55	4.400	0.420	7.748

of the near-corner CFD grid distribution is shown in Fig. 3-bottom. Varying geometries and mesh topologies cannot be
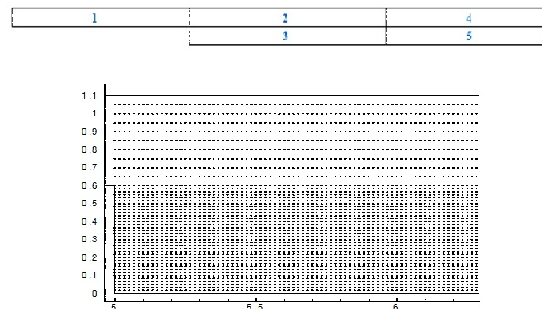

Fig. 3. Top: overview of a typical CFD domain with the different zones. Bottom: grid points distribution in the vicinity of the step for the case $H = 0.5$.

used in a standard POD, which requires a fixed geometry (with fixed mesh points). Thus, a *virtual geometry* is first defined as the case with a step size $H = 0.3$. In this, a *virtual mesh* is defined as the Cartesian equispaced mesh with five zones that are the counterparts of the zones in the CFD meshes. In both cases the x-y spacing between mesh points is as follows: zone 1: 0.1 x 0.05, zone 2: 0.01667 x 0.05, zone 3: 0.01667 x 0.01667, zone 4: 0.45 x 0.05, zone 5: 0.45 x 0.01667. Now, transformation between the virtual geometry and the actual geometries for each value of the step height H is done mapping the vertical coordinate, using the logarithmic function

$$\eta = A\ln(By + 1) \qquad (7)$$

where A and B are determined requiring that $\eta(H) = 0.3$ and $\eta(H + 0.5) = 0.8$, which preserves both the step and channel heights. The logarithmic function (7) has been selected because it exhibits a nearly linear growth in the upper part of the domain. Now, the state variables, u, v, p, and T must be transformed back and forth between the original and virtual meshes, which is done using the transformation (7) and cubic spline interpolation in both the original and virtual meshes.

B. POD + interpolation

N snapshots are computed with the CFD solver presented in [11] and must be representative of the parameter range we intend to cover, namely

$$(u_k, v_k, p_k, T_k) \quad \text{for } k = 1, ..., N. \tag{8}$$

Each snapshot gives the steady state of the system for a specific set of values of the parameters. These snapshots are first projected into the virtual geometry using (7) and then used to obtain the POD modes, which are calculated independently for each variable. For instance, POD modes for the horizontal velocity are given by

$$U_j = \sum_{k=1}^{N} \alpha_j^k u_k, \tag{9}$$

where the coefficients α_j^k are such that $(\alpha_1^1, ..., \alpha_1^N), ..., (\alpha_N^1, ..., \alpha_N^N)$ are the eigenvectors of the positive definite, symmetric NxN-matrix R, known as the *covariance matrix*, defined as

$$R_{ij} = \langle u_i, u_j \rangle \tag{10}$$

where Ω is the following *projection window* in the virtual geometry.

$$\Omega : 6 < x < 10, \quad 0 < y < 0.8, \tag{11}$$

Note that we are not taking the whole fluid domain to calculate POD modes, which would be quite computationally expensive. This simplification has been explained and checked in reference [2]. Now, if the expansion (9) is truncated to $n \le N$ terms, then the relative, root mean square (RMS) error is bounded by

$$|\text{error}| \le \sqrt{\sum_{i=n+1}^{N} \gamma_i \Big/ \sum_{i=1}^{N} \gamma_i} \tag{12}$$

where $\gamma_1 \ge ... \ge \gamma_N \ge 0$ are the eigenvalues of the covariance matrix (10). This gives an a priori estimate of the number of POD modes that must be retained to obtain a fixed error. After truncation and projection back into the CFD geometry, the POD modes are used to calculate the flow variables as

$$u(x, y) = \sum_{i=1}^{n_1} A_i^1 U_i(x, y) \quad v(x, y) = \sum_{i=1}^{n_2} A_i^2 V_i(x, y)$$
$$p(x, y) = \sum_{i=1}^{n_3} A_i^3 P_i(x, y) \quad T(x, y) = \sum_{i=1}^{n_4} A_i^4 T_i(x, y) \tag{13}$$

where the POD-mode amplitudes $A_i^1, ..., A_i^4$ are unknowns to be determined below. As an initial guess for the optimization process below, we shall use a first approximation of the amplitudes for arbitrary parameter values using POD + interpolation [1]; see also [6], [9] for related combinations of POD like methods and interpolation. The amplitudes of the modes (in terms of these parameters) are calculated in two steps: (a) at the parameter values associated with the snapshots, the POD-mode amplitudes $A_i^j = A_i^j(Re, T_{wall}, H)$ are obtained by just projecting the snapshots (8) into the POD basis, which requires projecting back and forth into the virtual mesh; and (b) at the remaining (intermediate) values of the parameters, each mode amplitude is calculated using

POD to obtain joint modes associated with dependence on the three parameters and cubic spline interpolation in each of these joint modes; see [1] for more details.

C. The overall residual

As anticipated above, the next step consists in calculating the POD-mode amplitudes (i.e. the coefficients in the expansions (13)) by minimizing the following residual (see [2])

$$\text{Residual} = \sum_{j=1}^{4} \frac{1}{N_E} |E_j(x_k, y_k)|$$
$$+ \sum_{j=1}^{4} \frac{1}{N_{BC}} |BC_j(x_k, y_k)|, \tag{14}$$

where (x_k, y_k) are all points in the following projection window

$$6 < x < 10 \quad 0 < y < 0.5 + H \tag{15}$$

which is the counterpart of the projection window in the virtual geometry that was used above to calculate POD modes (cf eq.(11) and see Fig. 2); E_j are the left hand sides of eqs. (1)-(4) and

$$BC_1 = u(p, y_{middle})$$
$$-\left\{ -24(y_{middle} - H)\left[(y_{middle} - H) - \tfrac{1}{2}\right] \right\}, \tag{16}$$

$$BC_2 = \frac{\partial p}{\partial x} - \left(-\frac{48}{Re} \right) \approx \frac{\Delta p_{in}}{\Delta x_{in}} - (-\frac{48}{Re}), \tag{17}$$

$$BC_3 = T(0, y_{middle}) - T_{entrance}, \tag{18}$$

$$BC_4 = T(x_{heating}, y_{middle}) - T_{wall} \tag{19}$$

account for the expressions that are set to zero in the non-homogenous boundary conditions at the walls. Now even though using a projection window instead of the whole fluid domain bears a saving in computational effort, the first term in (14) still involves all mesh points in the projection window and can lead to fairly expensive calculations if N_E is large. Here, as in [2] we proceed in a less standard way, noting that the essence of the POD method is that all snapshots are well approximated by a small number of modes, which suggests that the residual could be calculated using only information from a also small number of mesh points, somewhat larger than the expected number of POD modes. In the sequel, we only consider 50 equispaced points in the projection window to calculate the residual (14). Since the focus of this work is on the development of a ROM methodology with variable geometry, a robust (if not particularly efficient) optimization approach has been selected: the genetic algorithm. The parameters of the genetic algorithm used to compute the amplitudes in the modal expansions were: 10 bits per individual, 10,000 individuals in each population, 100 elite individuals that go over to the next generation, a crossover probability of 0.8, and a mutation probability such that 1% of individuals mutate one random bit. The CPU time needed to reach the solution with 15 modes (Tables III and V) in a 3.20 GHz desktop computer was 3 to 7 minutes depending on the test case. It should be noted however that this time can be reduced if the number of generations is lowered; the number of generations used was chosen to overshoot the necessary amount.

TABLE II
RELATIVE ERRORS IN % RESULTING FROM BOTH POD+INTERPOLATION
AND ROM CALCULATIONS ON THE FIGURES OF MERIT, USING 210
SNAPSHOTS AND RETAINING 15 MODES. POD MODES ARE CALCULATED
IN THE PROJECTION WINDOW (11) AND THE RESIDUAL IS CALCULATED
FROM 50 EQUISPACED POINTS IN THE PROJECTION WINDOW (15).

Test point	POD+interpolation			ROM		
	L_R	P_{drop}	Q'	L_R	P_{drop}	Q'
P01	0.0	0.5	0.4	1.9	0.4	0.1
P02	1.1	0.2	2.1	1.1	0.1	2.2
P11	10.5	3.6	0.0	10.5	2.5	4.0
P12	8.7	3.4	0.5	13.0	2.4	0.4
P13	0.8	2.8	0.5	0.0	1.0	1.0
P14	0.8	2.8	0.1	0.8	7.1	0.2
P15	14.6	1.8	1.3	17.1	1.4	1.3
P16	14.3	1.7	1.2	14.3	0.9	1.0
P17	1.5	0.5	6.7	1.9	0.5	8.4
P18	0.4	0.5	2.2	0.4	0.3	2.0

IV. RESULTS

To begin with, the ROM developed above is applied retaining the 15 most energetic POD modes calculated from the above defined 210 snapshots, using the projection window (11); the residual is calculated using only 50 equispaced points in the projection window (15). Relative errors (in %) on the three figures of merit at the test points are qiven in Table II as calculated using both POD+interpolation and the ROM; see Table I for the definition of the test points and the CFD calculated values of the figures of merit. Note that both POD+interpolation and ROM errors are always smaller than 4%, except for the reattachment length at test points P11, P12, P15, and P16 and the heat flux at test point P17. The reason for this lower accuracy seems to be due to the fact that POD approximations tend to deteriorate when either:

a) The step height is small (test points P11, P12, P15, and P16, see Table 1) because flow structures have a much smaller size than for larger values of H.
b) Or the wall temperature is lowest (test point P17), because heat transfer in this case is associated with small values of the heat flux near the walls.

In both cases, the actual numerical resolution in POD might be not sufficient. In order to deal with this difficulty, two improvements have been made in the method:

1) Increasing the number of snapshots with 35 additional ones at a step height H = 0.15. Results are given in Table III and show that results improve everywhere. Also, errors are now smaller than 2.4 % (including the approximation of L_R at P15 and P16), except for the reattachment length at P11 and P12 and the heat flux at P17, which are exact only within 8.7%. In any event, deviations of this order are admissible from the point of view of, for example, micro-electro-mechanical systems (MEMS) design engineering applications since, in this context, experimental work has uncertainties of the order of ±10%.
2) Using the same 245 snapshots as in case (a), but retaining twice the number of modes (a total of 30, instead of 15). The results obtained are presented in

TABLE III
SAME AS TABLE II, BUT USING 245 SNAPSHOTS

Test point	POD+interpolation			ROM		
	L_R	P_{drop}	Q'	L_R	P_{drop}	Q'
P01	0.9	0.4	1.4	0.0	0.1	2.0
P02	1.1	0.2	2.4	1.1	0.2	2.5
P11	5.2	2.6	0.7	5.2	1.7	0.3
P12	4.4	2.5	0.1	8.7	1.2	0.2
P13	0.8	2.8	0.2	1.7	0.9	0.5
P14	0.8	2.8	0.1	0.8	0.6	0.3
P15	0.0	0.3	1.3	0.0	0.1	1.3
P16	2.0	0.4	0.8	2.0	4.0	5.4
P17	1.5	0.5	6.9	1.9	1.2	7.5
P18	0.4	0.5	2.4	0.4	0.2	2.1

Table IV, and show that now accuracy is quite good for the three figures of merit in the ten test points. Also, results obtained using the ROM (within 1.5% accuracy) are consistently better than those obtained using POD+interpolation (2.8% errors). It is to be noted, however, that this improvement came at the expense of a larger computational time. While each run of the ROM in Table III is performed in only 3-7 CPU minutes, each run in Table IV requires 10-30 minutes.

TABLE IV
SAME AS TABLE II, BUT USING 245 SNAPSHOTS AND 30 MODES

Test point	POD+interpolation			ROM		
	L_R	P_{drop}	Q'	L_R	P_{drop}	Q'
P01	0.9	0.4	0.2	0.9	0.2	0.1
P02	1.7	0.2	0.6	1.7	0.0	0.6
P11	0.0	2.5	0.5	0.0	1.5	0.5
P12	0.0	2.5	0.3	0.0	1.3	0.3
P13	0.8	2.8	1.0	0.8	1.4	1.0
P14	0.8	2.8	0.2	0.8	1.1	0.4
P15	0.0	0.2	0.7	0.0	0.2	0.3
P16	0.0	0.1	0.0	0.0	0.1	0.0
P17	0.0	0.5	3.0	0.0	0.4	2.2
P18	0.0	0.5	1.0	0.0	0.4	1.0

Now, the question is whether a similar agreement is found when flow variables are compared at the local level. Figure 4 shows the streamline patterns in the step vicinity for test cases P01 and P17. Note that the agreement is quite good. The associated isobars and isotherms are given in Figs. 5 and 6, respectively. Agreement is again quite good, except of course at those regions where either pressure or temperature is almost constant, as was to be expected. POD modes and the residual were calculated using data from the projection windows (15) and (11), which excluded that zone where the flow exhibits a second recirculation bubble at some test points. It is also noteworthy that only five of the snapshots exhibited the second recirculation bubble, and that the CFD grid nodes were fairly sparse in that zone were the second bubble appears. In spite of these, the second recirculation bubble is reasonably well approximated. Still,
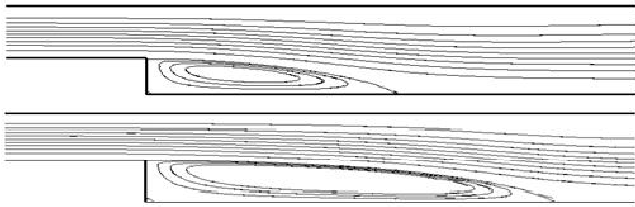
Fig. 4. Comparison between CFD (solid) and ROM (dashed) streamlines at test points P01 (top) and P17 (bottom)
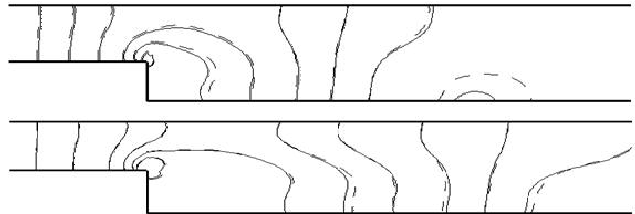

Fig. 5. Comparison between CFD (solid) and ROM (dashed) isobars at test points P01 (top) and P17 (bottom)
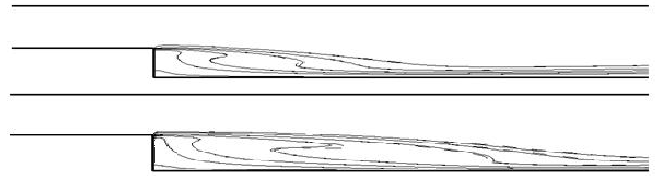

Fig. 6. Comparison between CFD (solid) and ROM (dashed) isotherms at test points P01 (top) and P17 (bottom)

in the virtual and CFD geometries, respectively. Also, the residual is calculated taking 50 and 15 points in the first ($6 < x < 10$) and second ($9 < x < 13$) sub-windows, respectively. Results are shown in Table 5-right and are quite similar to those resulting from the first improvement above, which shows that the whole process is quite robust.

TABLE V
TABLE 5 RELATIVE ERRORS % ON THE FIGURES OF MERIT CALCULATED WITH THE ROM DESCRIBED IN TABLE III, BUT (LEFT) USING 70+30 POINTS IN THE PROJECTION WINDOW (15), AND (RIGHT) USING TWO PROJECTION SUB-WINDOWS, SEE (11)-(21).

Test point	One window, 70+30 points			Two windows, 50+15 points		
	L_R	P_{drop}	$\tilde{Q}'$	L_R	P_{drop}	$\tilde{Q}'$
P01	0.9	0.2	0.9	0.9	0.2	0.6
P02	1.7	0.1	2.3	1.7	0.1	2.4
P11	5.2	1.9	0.2	5.2	1.7	0.5
P12	0.0	1.3	1.5	0.0	1.3	0.7
P13	0.8	0.9	0.1	1.7	0.9	0.0
P14	0.8	0.6	0.3	0.8	0.6	0.3
P15	0.0	0.1	1.2	2.4	0.2	1.1
P16	2.0	1.0	2.7	0.0	0.3	0.8
P17	1.1	0.5	7.6	1.1	0.5	7.6
P18	0.4	0.1	2.2	0.4	1.6	2.2

the main recirculation bubble is always well approximated even though the projection window excluded also the main recirculation bubble in some cases (Fig. 2-up) and a large part of this bubble in some other cases (Fig. 2-middle). All these illustrate both (a) the power of POD when this method is properly used and (b) the fact that the ROM is quite robust in the sense that selection of the projection window is not critical. Now, a question arises on whether the results above can be improved with a better selection of both the projection window and the points where the residual are calculated. Concerning the latter, note that choosing 50 equispaced points in the projection window (15), as we did in Tables II-IV to calculate the residual means that, for instance, that zone affected by the first recirculation bubble ($0 < y < H$) contains 18 points when $H = 0.1$ and 40 points when $H = 0.6$. This suggests two improvements:

- A first improvement results from maintaining the projection windows (15) and (11), but increasing the number of points in the residual calculation to 100, and ensuring that 70 of them are in that part of the projection window affected by the first recirculation bubble ($0 < y < H$). Results are shown in Table 5-left. Comparison with Table IV shows that a significant improvement results from the increase in the number of points and the better selection of the 100 points. Note that errors are within 2.3% except for the reattachment length at point P11 and the heat flux at point P17; but note that the CFD values of and heat flux at these points are quite small, which explains the larger relative errors.

- The projection window can be split into two sub-windows in such a way that they roughly cover those regions affected by the recirculation bubbles. Namely,

$$6 < x < 10, 0 < \eta < 0.3; 9 < x < 13, 0.3 < \eta < 0.8 \quad (20)$$

$$6 < x < 10, 0 < y < H; 9 < x < 13, 0.5 < y < H \quad (21)$$

V. CONCLUSIONS

A method has been presented to generate ROMs in fluid-thermal problems with variable geometry. In particular, the required CFD-calculated snapshots are obtained in computational domains with variable shape and number of grid points. The results obtained show that the method is flexible, robust, and accurate enough to be used for practical engineering applications. In particular, three parameters are considered in the test problem, namely the Reynolds number, the wall temperature, and the step height, which could be considered as representative of a variety of industrial problems in which flow topology, thermal, and geometry properties need to be analyzed simultaneously. Some remarks about the results are now in order:

1) When considering test points located well inside the 3-D parametric space (test points P1 and P2), the ROM global results (main recirculation region reattachment length, pressure drop, and heat flux) are within 2% of the CFD solution even with the simplest ROM configuration (210 snapshots, 15 POD modes, and residual calculated using 50 equispaced points in the

simplest projection window). The spatial distribution of the flow variables is also close enough to the CFD solution to be used for detailed analysis purposes. The CPU time needed to generate each of these ROM results is of the order of 3 minutes, which is much smaller that the time needed to generate a CFD solution (of the order of 8 to 10 hours).

2) The accuracy of the method degrades, as it could be expected when the selected test points are close to the boundary of the 3-D parametric space. In this case, discrepancies with the CFD solutions using the simplest ROM configuration (Table II) are of the order of 3% except at some points where they can be as large as 17%. The time needed to generate the ROM model goes up to about 7 minutes. Adding some snapshots in the region of lower step height (Table III) reduces the largest errors to 8.7%, which it is already acceptable for engineering purposes and still requires a CPU time of 7 minutes, which is quite competitive when compared to the time needed to generate a full CFD solution.

3) Accuracy can be increased either retaining more POD modes (30 instead of 15, see Table IV), which gives excellent accuracy but requires a CPU time of 10-30 minutes (still competitive compared to CFD) or selecting better both the projection window and the points where the residual is calculated (Table V). This gives both an excellent precision (errors within 3% except at those points where the approximated quantities are really small, where it is still reasonable, of the order of 7%) and a fairly small CPU time (3-7 minutes). Concerning the latter improvement, it is convenient that the projection window includes at least a part of the structured flow regions (e.g., second recirculation bubble), and that the selected points to calculate the residual are located in a balanced way, namely that there is a sufficient amount of them in the most structured regions. Nevertheless, the method is robust enough in connection with all these guidelines since, for instance reasonable results (even in the second recirculation bubble) are obtained selecting a projection window that does not contain the second recirculation bubble (or even does not contain the first recirculation bubble either, see Fig. 2), and calculating the residual using equispaced points in the first projection window, which puts only a few points in the first recirculation bubble.

4) For simplicity, we have retained the same number of POD modes in each flow variable, but this can of course be improved selecting an appropriate number of modes for each flow variable. This could be done in an efficient way using the a priori error estimate (12), which is based on the singular values of each POD.

5) Adding 15 additional snapshots in that region of the parameter space where the ROM results exhibited largest errors highly improves the efficiency at a reasonable computational cost. This opens the possibility of designing a method to select the snapshots in such a way that only a few of them are enough, if properly selected. Its number should be just somewhat larger than the number of POD modes (say, twice the number

of modes). The method would provide a dramatic reduction in computational time since it is essentially associated with the CFD calculations of the snapshots. The remaining calculations in the method are quite inexpensive after the improvements introduced above.

6) Gradient like methods could be used to dramatically decrease computational time, which as explained above would require a redefinition of the residual and an efficient calculation of the gradient. Some care should also be taken with non-uniqueness of local minima of the residual, which is under research.

REFERENCES

[1] D. ALONSO, A. VELAZQUEZ, AND J. VEGA, *Robust reduced order modeling of heat transfer in a back step flow*, Int. J. Heat Mass Tran., 52 (2008), pp. 1149–1157.

[2] ——, *A method to generate computationally efficient reduced order models*, Comput. Method. Appl. M., 198 (2009), pp. 2683–2691.

[3] J. S. R. ANTTONEN, P. I. KING, AND P. S. BERAN, *Pod-based reduced-order models with deforming grids*, Math. Comp. Model., 38 (2003), pp. 41–62.

[4] B. F. ARMALY, F. DURST, J. C. F. PEREIRA, AND B. SCHÖNUNG, *Experimental and theoretical investigation of backward-facing step flow*, J. Fluid Mech., 127 (1983), pp. 473–496.

[5] D. BARKLEY, M. GOMES, AND R. HENDERSON, *Three dimensional instability in flow over a backward facing step*, J. Fluid Mech., 473 (2002), pp. 167–190.

[6] T. BUI-THANH, *Proper Orthogonal Decomposition Extensions and their Applications in Steady Aerodynamics*, Master Thesis. Singapore-MIT Alliance, 2003.

[7] F. DURST AND J. C. F. PEREIRA, *Time-dependent laminar backward-facing step flow in a two dimensional duct,*, J. Fluid. Eng., 110 (1988), pp. 289–296.

[8] J. HOLLKAMP AND R. GORDON, *Reduced-order models for nonlinear response prediction: Implicit condensation and expansion*, J. Sound Vib., 318 (2008), pp. 1139–1153.

[9] L. LORENTE, J. VEGA, AND A. VELAZQUEZ, *Generation of aerodynamic databases using high order singular value decomposition*, J. Aircraft, 25 (2008), pp. 1779–1788.

[10] D. LUCIA, P. BERAN, AND W. SILVA, *Reduced-order modeling: new approaches for computational physics*, Prog. Aerosp. Sci., 40 (2004), pp. 51–117.

[11] B. MENDEZ AND A. VELAZQUEZ, *Finite point solver for the simulation of a 2-d laminar incompressible unsteady flows*, Comput. Method. Appl. M., 193 (2004), pp. 825–848.

[12] M. P. MIGNOLET AND C. SOIZE, *Stochastic reduced-order models for uncertain geometrically nonlinear dynamical systems*, Comput. Method. Appl. M., 197 (2008), pp. 3951–3963.

[13] S. NIROOMANDI, I. ALFARO, E. CUETO, AND F. CHINESTA, *Real-time deformable models of non-linear tissues by model reduction techniques*, Comp. Meth. Prog. BioMed., 91 (2008), pp. 223–231.

[14] Y. ROUIZI, Y. FAVENNEC, J. VENTURA, AND D. PETIT, *Numerical model reduction of 2d steady incompressible laminar flows: Application on the flow over a backward-facing step*, J. Comput. Phys., 228 (2009), pp. 2239–2255.

[15] W. A. SILVA AND R. E. BARTELS, *Development of reduced-order models for aeroelastic analysis and flutter prediction using the cfl3d v6.0 code*, J. Fluid. Struct., 19 (2004), pp. 729–745.

[16] A. VELAZQUEZ, J. ARIAS, AND B. MENDEZ, *Laminar heat transfer enhacement downstream of a backward facing step by using a pulsating flow*, Int. J. Heat Mass Tran., 51 (2008), pp. 2075–2089.

[17] J. VIERENDEELS, L. LANOYE, J. DEGROOTE, AND P. VERDONCK, *Implicit coupling of partitioned fluid-structure interaction problems with reduced order models*, Comp. Struct., 85 (2007), pp. 970–976.